Optimized Detection of Volatile Organic Compounds Utilizing Durable and Selective Arrays of Tailored UiO-66-X SURMOF Sensors

Salih Okur,[‖] Tawheed Hashem,[‖] Evgenia Bogdanova, Patrick Hodapp, Lars Heinke, Stefan Bräse, and Christof Wöll*

ABSTRACT: Metal−organic frameworks (MOFs), with their well-defined and highly flexible nanoporous architectures, provide a material platform ideal for fabricating sensors. We demonstrate that the efficacy and specificity of detecting and differentiating volatile organic compounds (VOCs) can be significantly enhanced using a range of slightly varied MOFs. These variations are obtained via postsynthetic modification (PSM) of a primary framework. We alter the original MOF's guest adsorption affinities by incorporating functional groups into the MOF linkers, which yields subtle changes in responses. These responses are subsequently evaluated by using machine learning (ML) techniques. Under severe conditions, such as high humidity and acidic environments, sensor stability and lifespan are of utmost importance. The UiO-66-X MOFs demonstrate the necessary durability in acidic, neutral, and basic environments with pH values ranging from 2 to 11, thus surpassing most other similar materials. The UiO-66-NH_2 thin films were deposited on quartz-crystal microbalance (QCM) sensors in a high-temperature QCM liquid cell using a layer-by-layer pump method. Three different, highly stable surface-anchored MOFs (SURMOFs) of UiO-66-X obtained via the PSM approach (X: NH_2, Cl, and N_3) were employed to fabricate arrays suitable for electronic nose applications. These fabricated sensors were tested for their capability to distinguish between eight VOCs. Data from the sensor array were processed using three distinct ML techniques: linear discriminant (LDA), nearest neighbor (*k*-NN), and neural network analysis methods. The discrimination accuracies achieved were nearly 100% at high concentrations and over 95% at lower concentrations (50−100 ppm).

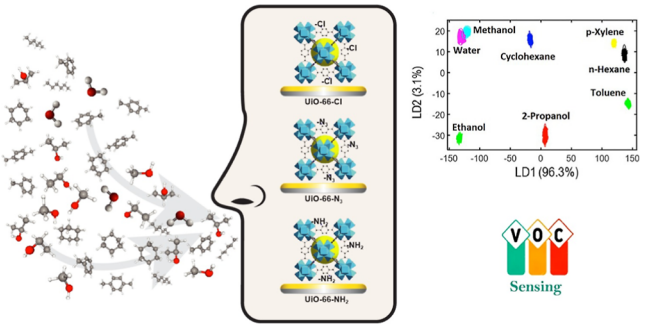

KEYWORDS: *VOC, discrimination, electronic nose, MOF, SURMOF, layer-by-layer, stability, harsh conditions*

Porous materials are particularly well suited to the fabrication of sensors that detect volatile organic compounds (VOCs). The uptake of molecules from the gas phase into such materials can be monitored in a straightforward fashion using gravimetric, optical, or electrical readout.[1−4]

In this context, metal−organic frameworks (MOFs) recently have attracted substantial attention as structurally well-defined systems with record values for their surface areas, large pore size and volume, and a highly modular structure.[5−7] In addition, a theoretical description of these porous materials is rather straightforward. Recent work has demonstrated the strong potential for MOFs to perform well in a wide variety of application fields.[8,9]

For most applications, it is highly beneficial to employ structurally well-defined monolithic MOF thin films. In this context, surface-anchored MOFs (SURMOFs) in particular offer a number of advantages.[10,11] These films are fabricated by using layer-by-layer (LBL) processes. In previous work, single-compound MOF thin films or MOF arrays have been successfully used to detect and discriminate between pure single-component gases, vapors, or liquids.[12−14] The reliable detection of multicomponent gases, however, is rare.

In this regard, electronic nose (e-nose) systems based on sensor arrays made from different MOF types are of particular interest. The multidimensional response of these arrays can be analyzed by using machine learning (ML) techniques. Several algorithms are available for such automatized data analysis, including principal component analysis (PCA), linear discriminant analysis (LDA), and k-nearest neighbor (*k*-NN).[15] The e-nose-based sensors are typical molecular systems with the potential to detect and discriminate several similar molecules. In fact, chiral MOFs able to discriminate between enantiomers have also been reported.[16−18]

Here, we focus on gravimetric e-nose sensors based on a quartz-crystal microbalance (QCM) array that allows for simultaneous discrimination of several different VOCs. The QCM was not only used for sensor readout but also for monitoring and optimizing the UiO-66-NH_2 SURMOF synthesis in a Teflon liquid cell with a pump system at elevated temperatures.[19] ML methods were then used to process the multidimensional response of the sensor array and determine the relative concentrations of the analytes for different VOCs.

In previous work, QCM-based sensor arrays employing a variety of materials, including different types of MOFs, were employed to detect and discriminate between odor molecules, plant essential oils, and VOCs.[16,20−23] However, in real-world applications, the sensing of MOF compounds often faces several obstacles because some of these MOFs are unstable in humid conditions due to corrosion by water vapor.[24−28] For instance, in the context of CO_2 gas separation from flue gas (water vapor: ∼10%−15%), thin films of the MOF (HKUST-1) have been reported to undergo changes in morphology and framework bonding.[29] For this reason, the degradation or even the change in properties of the MOF has to be considered with regard to fabrication of MOF-based sensor arrays for operation under harsh conditions.

We demonstrate here that UiO-66-NH_2 MOFs are well suited to such tasks. They perform well under harsh conditions due to their chemical, thermal, and architectural stabilities derived from their strong Zr−O bonds. The particulate nature of the standard form of MOFs, i.e., powders, is not well suited to the fabrication of gravimetric sensors and many other application fields.[11] Our group has pioneered the deposition of structurally well-defined iconic UiO-66-NH_2 SURMOFs on different substrates, followed by thin-film stability tests and employment of these SURMOFs in hydrogen separation.[30,31] A particularly important feature of these UiO-66-NH_2 SURMOFs results from the primary amine, which can be modified using postsynthetic modification (PSM)[32] to provide a wide variety of chemical or structural variants of multifunctional SURMOFs. For instance, the amino group in the pristine Zr SURMOFs can be converted to an azide (N_3) or a chloride (Cl), which endows the resultant functional Zr SURMOFs with high sensing performance toward the detection of specific target gases or liquids.

Our novel approach provides a sensor platform starting from a parent MOF, UiO-66-NH_2, which is postsynthetically functionalized to render specific sensing properties to the device. Since the same SURMOF is always deposited using optimized conditions, the variation in device performance is strongly reduced. Since the number of possible different functionalities that can be attached to the UiO-66-NH_2 SURMOFs is virtually infinite, our approach combines high sensor stability, sensitivity, and selectivity for a broad range of detection scenarios.

In this work, three highly stable UiO-66-X (X = NH_2, Cl, and N_3) SURMOFs were synthesized for e-nose applications. They were used to discriminate eight VOCs in the gas phase. The discrimination accuracies obtained using three statistical models—LDA, *k*-NN, and neural network analysis (NNA)—were more than 95% between 50 and 100 ppm and almost 100% at high concentrations.

MATERIALS AND METHODS

Surface Preparation. AT-cut quartz sensor crystals (0.3 mm thick) coated with a gold layer QSX 301 (100 nm thick) (Q-Sense, Frölunda, Sweden) with a resonance frequency at 4.95 MHz were first functionalized by immersion in an ethanolic solution of 11-mercapto-undecanol (MUD), producing a self-assembled monolayer (SAM) with an exposed OH-terminated stem.

Synthesis of SURMOFs. The functionalized gold-coated QCM sensors were installed in a commercial openQCM-D (Novatech, Italy) instrument equipped with a Teflon liquid cell. To protect sensitive components against dimethylformamide (DMF)-based solutions, Kalrez-type O-rings (DuPont, USA) were employed. The deposition of the UiO-66-NH_2 SURMOFs on the Au substrate was carried out in situ following previously described LBL protocols using a peristaltic pump (Ismatec, Wertheim, Germany). After pumping 1 mL of metal ion solution into a liquid cell and allowing one h for the reaction to occur with the functionalized surface, the cell was rinsed with 5 mL of DMF to eliminate excess unreacted metal ion clusters. The liquid cell was then filled with 1 mL of MOF linker solution, with 45 min allowed for the linker molecules to bind with the residual reacted Zr clusters on the surface to complete the reaction. This resulted in a functionalized surface. Lastly, the deposition cycle of the SURMOF layer was completed by rinsing with pure DMF that was pumped through the liquid cell a second time to eliminate any unreacted linker molecules (Figure 1). The SURMOFs used were grown using a total of 30 deposition cycles,. All of the synthesis processes and the data acquisition were coordinated by a program written in Python.

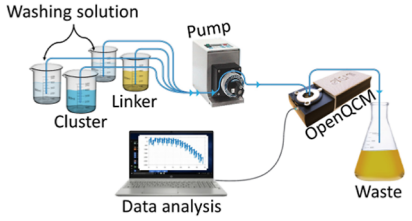

Figure 1. A schematic illustration of the working principle of the one-channel openQCM for SURMOF synthesis.

CHARACTERIZATION

All functional UiO-66-X SURMOF samples (X = NH_2, N_3, and Cl) were characterized by X-ray diffraction (XRD) using a Bruker D8-Advance "DaVinci" (Ettlingen, Germany) in Bragg−Brentano geometry and a 192-stripe Lynxeye detector with Cu Kα_1 radiation (λ = 1.54 Å).

In addition, scanning electron microscopy (SEM) measurements utilizing a FEI Philips XL 30 field-emission gun environmental scanning electron microscope (FEG-ESEM) (FEI Co., Hillsboro, OR, USA) allowed us to explore the morphologies of the SURMOFs. Before SEM imaging, each sample was coated with a thin layer (3−5 nm thick) of gold/palladium film to protect it from charging. The measurements were conducted under high vacuum with an acceleration voltage of 20 keV.

Infrared reflection absorption spectroscopy (IRRAS) spectra of all functional UiO-66-X SURMOF samples were obtained by using a Bruker Vertex 80 spectrometer (Germany). The IRRAS data were collected at room temperature using grazing incidence (80°) geometry, and a resolution of 4 cm^{-1} was achieved by accumulating 2048 scans.

Postsynthetic SURMOF Refunctionalization. The UiO-66-NH_2 SURMOF-coated QCM crystal sensors were modified in a Sandmeyer reaction-type two-step procedure to obtain the

corresponding azide (UiO-66-N_3) or chloride (UiO-66-Cl) functionalized QCM sensors.

First Step: Diazonium Salt Formation. The diazonium-salt-functionalized SURMOF was prepared by diazotization from a UiO-66-NH_2 SURMOF-coated QCM crystal sensor.

A solution of 500 mg of sodium nitrite (7.23 mmol) in 15 mL of deionized water was cooled to 0 °C, and 3 mL of 6 M HCl was slowly added. Maintaining the solution at 0 °C and under slow but constant stirring, the UiO-66-NH_2 SURMOF-coated QCM crystal was submerged in the solution for 15 min using a custom-machined PTFE holder. This holder exposes the SURMOF-coated surface to the solution while holding the QCM crystal steady in the stirred solution and prevents mechanical damage to the SURMOF coating. The SURMOF-coated QCM sensor was then carefully rinsed with deionized water and placed in a beaker with deionized water for 1 min. After rinsing for a second time with deionized water, the diazonium-salt-functionalized SURMOF was directly subjected to the second reaction step without further treatment or drying.

SECOND STEP

Azide Functionalization. The azide-functionalized SURMOF was prepared from the diazonium salt-functionalized SURMOF-coated QCM crystal sensor.

The diazonium-salt-functionalized SURMOF-coated QCM crystal was added to a solution of 1.30 g of sodium azide (20.0 mmol) in 20 mL of deionized water cooled to 0 °C. The QCM crystal was prepared in the first reaction step using the same PTFE holder described in the first step. The sensor was kept in the solution under slow but constant stirring at 0 °C for 5 min before removing the ice bath and allowing the solution to slowly warm to room temperature. After two hours, the QCM crystal was removed from the solution, rinsed with deionized water, placed in a beaker with deionized water for 2 min, and then rinsed a second time with deionized water. Excess water was carefully blown off the sensor in a nitrogen gas stream, and the sensor was dried in an oven at 40 °C overnight.

Chloride Functionalization. The chloride-functionalized SURMOF was prepared from the diazonium salt-functionalized SURMOF-coated QCM crystal sensor.

We added 1.98 g of copper(I) chloride (1 mol/L) to a beaker with 20 mL of deionized water and cooled it to 0 °C under constant stirring. The freshly prepared diazonium-salt-functionalized SURMOF-coated QCM sensor was then submerged in the solution using the PTFE holder described in the first step. The cooling bath was then removed, and the solution was allowed to slowly warm to room temperature. After two h, the QCM sensor was removed and carefully rinsed with deionized water, placed in a beaker of deionized water for two min, and then rinsed a second time with more deionized water. Excess water was then carefully blown off in a nitrogen gas stream, and the sensor was dried in an oven at 40 °C overnight.

The modified SURMOFs were subjected to a comprehensive characterization utilizing infrared reflection absorption spectroscopy (IRRAS) to validate the efficacy of the modification process. As evidenced in Figure S2, the results unequivocally substantiate the success of the modification procedure.

Gas Delivery System and VOC Measurements. Figure S1 depicts our homemade four-channel QCM-type e-nose experimental setup for VOC measurements with three functionalized UiO-66-X SURMOFs equipped with a gas delivery setup. The test cell was constructed from four openQCM Teflon cells connected in series with Teflon tubes (1 mm diameter). Three of the four units were used to realize the functional UiO-66-X sensors (X: NH_2, N_3, and Cl). The remaining unit used a bare QCM sensor with a gold surface as a control channel. There were two mass flow controllers connected in parallel between the argon (Ar) source and the test cell. One of them was used to flash the test cell with Ar for purging the residue of VOC inside, and it also directly controlled the Ar flow during the dilution of the VOC concentration. The other mass flow controller determined the rate of flow passing through the liquid inside the VOC bubbler that transported the saturated VOC gas just above the surface to the test cell. The VOC concentration inside the test cell was obtained by multiplying the saturated value of the concentration with the ratio of the flow rates of these two mass flow readings. The saturated values of each gas were calculated from the well-known Antoine parameters[33] at room temperature (20 °C). Table 1 shows the calculated saturation concentrations for eight targeted VOC analytes. The same openQCM-D Teflon liquid cells used for high-temperature SURMOF synthesis were also employed for VOC tests in gas (Figure S1a) phases. The temperature was kept constant at room temperature (20 °C) to prevent small temperature fluctuations during the VOC test measurements.

Table 1. Calculated Concentrations under Saturated Pressures of Eight VOCs Used for Gas Adsorption Measurements at Room Temperature (25 °C)

VOCs	c_{sat} (ppm)
ethanol	68,776.3
water	23,531.6
cyclohexane	117,210.5
2-propanol	50,684.2
methanol	150,328.9
p-xylene	12,907.9
toluene	27,631.6
n-hexane	182,381.6

For the evaluation of the QCM data (both SURMOF deposition and sensing), we employed the linear relationship between resonance frequency and the mass upload (Sauerbrey equation)[34]

$$\Delta m = -\frac{A\sqrt{\rho\mu}}{2f_0^{\,2}}\frac{\Delta f}{n} = -C\frac{\Delta f}{n} \quad (1)$$

where Δm is the change in mass, Δf is the measured frequency shift, and f_0 is the fundamental frequency of the quartz crystal before a mass change. Therefore, a change in the mass results in a frequency change. Consequently, C is usually defined as the mass sensitivity constant related to the structural and physical properties of the oscillating quartz QCM substrate and the driving fundamental resonance frequency.[34,35] For a 5 MHz crystal, C = 17.7 ng/(cm^2·Hz). The parameter n is the number of the odd harmonic and can be 1, 3, 5, 7, etc. This equation allows us to calculate the mass upload of the thin film during the synthesis of UiO-66-NH_2 or the amount of VOC gas absorbed by the SURMOF upon exposure to the corresponding gases.

Two concentrations were applied for the gas phase adsorption measurements to eight VOCs, including water vapor. The first adsorption measurement was conducted at high concentrations of VOCs under their saturated pressures, as given in Table 1. Each VOC gas was injected into the gas test cell for 10 min for adsorption and then flashed with inert Ar gas for 10 min for desorption. These adsorption and desorption cycles were repeated four times to test repeatability. For the second measurement, solutions with six different low concentrations (10, 15, 25, 50, 75, and 100 ppm) were chosen to identify the detection limit of the functional UiO-66-X SURMOF sensor films. In this case, the gas injection time was lowered again to 10 min for adsorption, but the Ar rinsing time was increased to 20 min for desorption to examine the sensor response time.

Data Analysis. The control of the entire setup, data acquisition, and e-nose data analysis were conducted with a program code written in MATLAB 2021B. Two standard supervised ML algorithms, LDA[16,36] and *k*-NN,[16,22] as described in previous work,[16,22,36] were used to classify the sensing data for e-nose discrimination analysis. During data analysis, the data in the saturated region (highest response region) of the adsorption−desorption curves were used to increase accuracy. A 10-fold cross-validation process was employed for the classification analysis. Typically, 90% of the total observations were used for the training set and 10% were used for testing the discrimination accuracies. The obtained results were listed as a confusion matrix to present the discrimination analysis results of LDA, *k*-NN, and NNA models.

RESULTS AND DISCUSSION

Synthesis of UiO-66-NH_2 SUR MOF Films with the Layer-by-Layer Method Using a High-Temperature QCM-D Liquid Cell. The synthesis parameters, such as temperature, injection and exposure times, flow rates, and metal ion/cluster concentration, as well as the organic linker and rinsing solutions, directly affect the growth kinetics of the UiO-66-NH_2 SURMOF films. The growth of these films on MUD SAMs was monitored using a QCM. Figure 2 presents

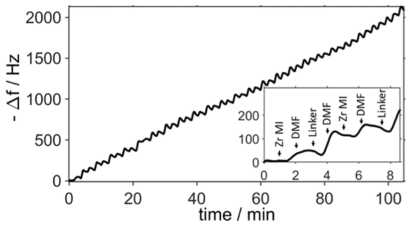

Figure 2. Typical temperature and time-dependent synthesis kinetics of UiO-66-NH_2 SURMOF films with the LBL method using a high-temperature QCM-D liquid cell.

the typical time-dependent synthesis kinetics of UiO-66-NH_2 SURMOF films with the LBL method using a high-temperature QCM-D liquid cell at 100 °C. In this case, a short injection time of 7.5 s was chosen for both solutions of Zr metal clusters and linker with continuous flow. In between, 2 min of DMF rinsing was applied through the MUD-coated QCM substrate inside the liquid cell for each cycle for fast SURMOF film formation. Typically, −2100 Hz (37 $\mu g/cm^2$, e.g., 57.5 μg with 1.54 cm^2 Q-Sense QCM substrate surface area) UiO-66-NH_2 thin mass upload was obtained with 26 cycles. In this synthesis, the temperature was kept constant at 100 °C. A linearly increasing upload during synthesis was observed with an increasing LBL cycle. A linear fit provides an −19.2 Hz/min synthesis upload speed and −2100 Hz in total for 26 cycles.

Figure S3 displays the structural analysis, and Figure S3a depicts the XRD pattern of the functional UiO-66-X after postmodification to exchange the functional groups between NH_2, N_3, and Cl. XRD peak positions at 7.4° representing (111) and at 8.5° at (200) orientation and intensities are fully consistent with simulations of the previously reported UiO-66-NH_2 bulk structure.[19,30,37] SEM imaging was conducted to analyze the topography of the synthesized sensors. Figure S3b displays SEM images of the top surface, and Figure S3c shows a cross-sectional view for the structural analysis of UiO-66-NH_2 SURMOF films. The SEM surface topography presents smooth crystalline UiO-66-NH_2 SURMOF films covering the whole QCM surface with approximate thicknesses of 300−500 nm.

Stability Test. To evaluate the stability of our sensors, the modified system underwent pre- and postexposure analysis to saturated hot water vapor under controlled conditions of 90 °C and 120 min. Figure 3a,b shows the ethanol uptake results before and after saturated hot water vapor at a relative humidity condition of 90 °C, respectively. The results demonstrate the high stability of our system. Slight changes were observed following exposure to the hot water vapor, since hot water molecules can easily diffuse through the empty pores during long exposure, and they cannot be easily recovered in short period of time. To recover the water molecules completely, the temperature of the films should be increased above 100 °C and annealed sufficiently long in a N_2 environment.

The mass uptake drops with an increasing temperature due to a lower concentration of water molecules inside the cell. This is because the relative humidity inside the cell is proportionally related to the concentration of the water molecules. However, the water molecule concentration is inversely related to the environmental temperature according to the general gas law as long as the pressure and volume are kept constant. The QCM sensor adsorption test results show repeatable cycles even at high temperatures up to 90 °C and high-humidity vapor conditions up to 100% relative humidity. XRD results before and after high humidity tests (Figure 3c,d) indicate that the functionalized UiO-66-X sensors remain structurally stable at high humidity.

Adsorption Measurements under Saturated VOC Concentrations. Eight VOCs were tested at high and low concentrations. The first adsorption measurement of VOCs was conducted at a high concentration under their saturated pressures, as given in Table 1. Each VOC gas was injected into the gas test cell for 10 min for adsorption and then flushed with inert Ar gas for 10 min for desorption. These adsorption and desorption process cycles were repeated four times to test repeatability. The second measurement was performed at low concentrations (10, 15, 25, 50, 75, and 100 ppm) to find the limit of detection (LOD) of functional UiO-66-X SURMOF sensor films. The gas injection time was again kept to 10 min for adsorption for quick tests toward practical applications. For desorption, the Ar rinsing time was chosen to be 20 min.

Figure 4 displays the negative QCM frequency changes as a result of mass uploads on the three functional UiO-66-X SURMOF sensors when exposed to eight VOCs, with X =

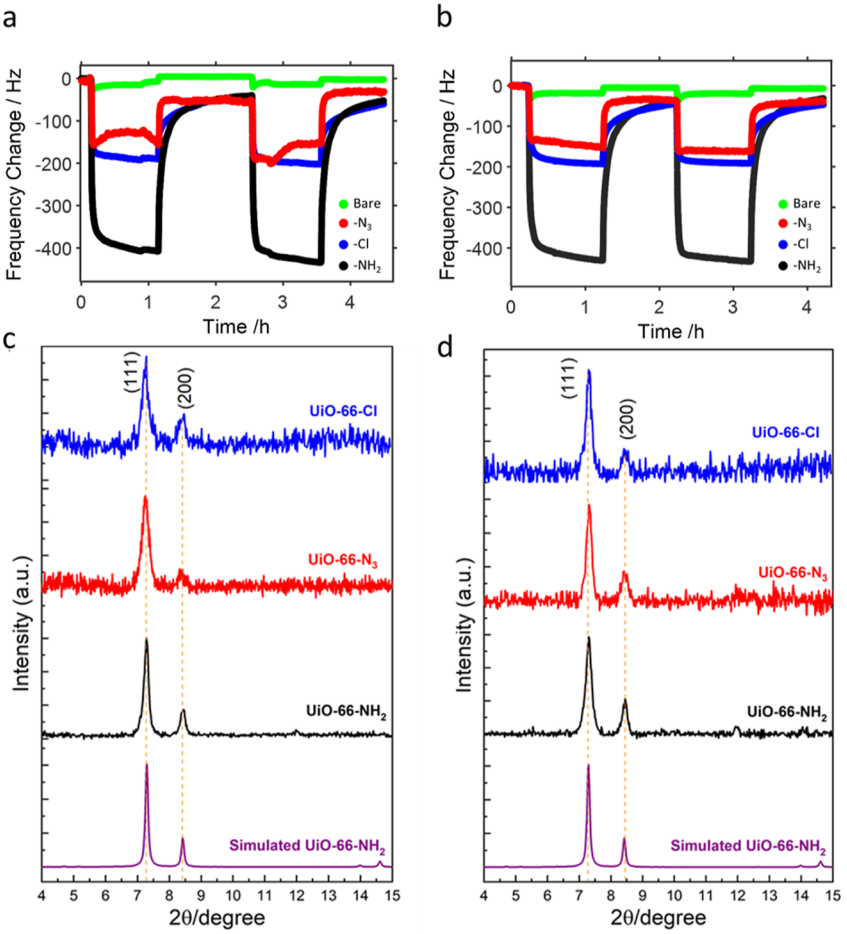

Figure 3. Ethanol uptake results (a) before and (b) after saturated hot water vapor at relative humidity conditions at 90 °C. XRD results of UiO-66-X (c) before and (d) after a high-humidity test (100% RH at 90 °C).

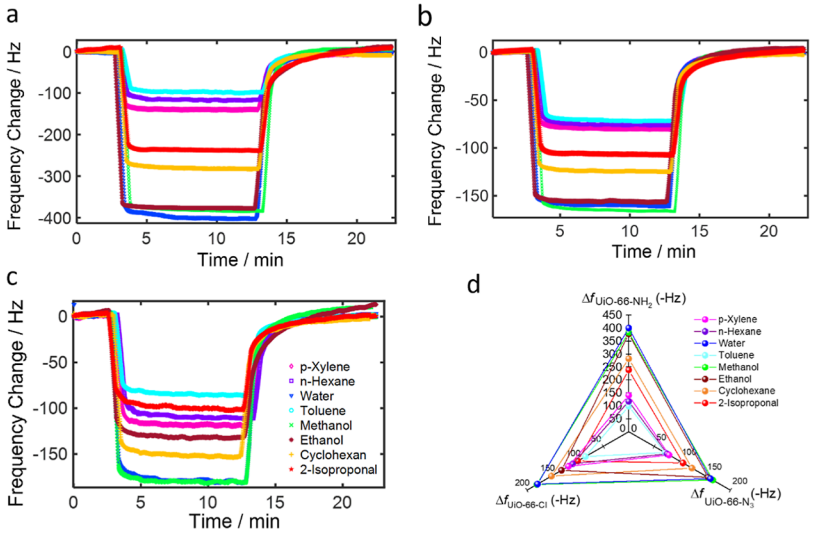

Figure 4. Negative QCM frequency changes observed due to mass uploads on three functional UiO-66-X SURMOF sensors with X = NH_2 (a), X = Cl (b), and X = N_3 (c) when exposed to eight VOCs. Each analyte underwent four cycles with 10 min absorption and 10 min desorption times. UiO-66-X demonstrated a response time of less than 1 min. The radar plot in Figure 4d illustrates the maximum sensor responses against each VOC gas.

NH_2 (Figure 4a), X = Cl (Figure 4b), and X = N_3 (Figure 4c). Each analyte was tested with four cycles with 10 min adsorption and 10 min desorption times. The response time of UiO-66-X was less than 1 min, and the radar plot in Figure 4d displays the maximum of the sensor responses against each VOC gas.

The adsorption tests at a high concentration indicated that the response times of the sensors were less than 1 min, and

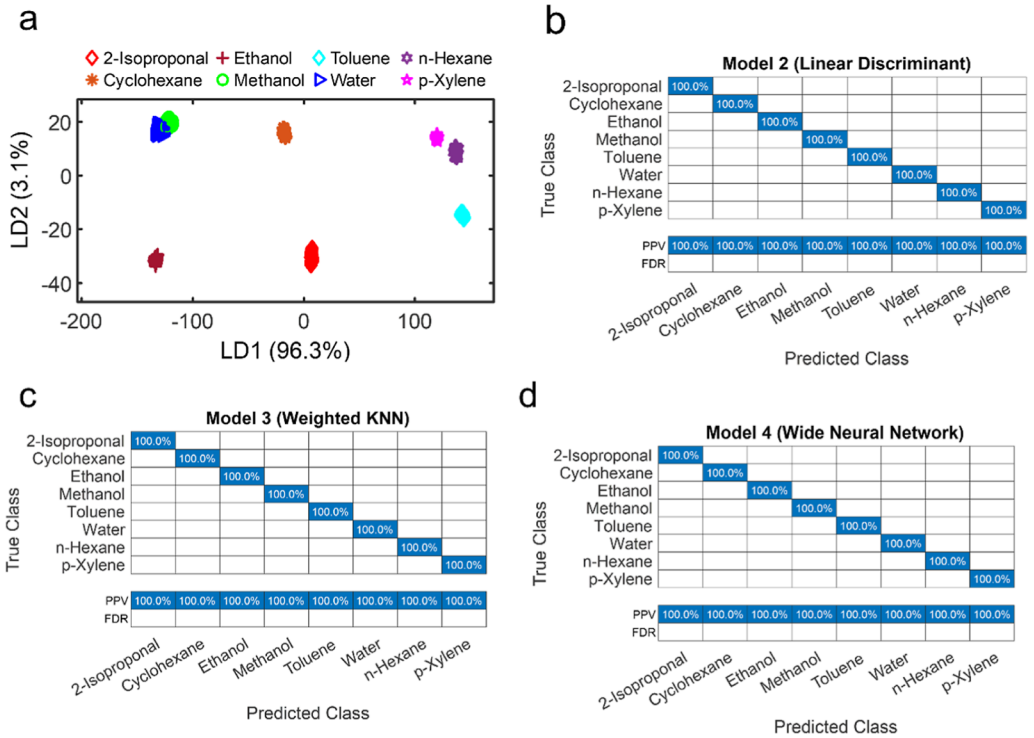

Figure 5. E-nose analysis results. (a) Two-dimensional plot of LDA with a 95% confidence ellipse of eight VOCs, including water, at their saturated vapor pressure concentrations. The confusion matrix results of the (b) LDA, (c) *k*-NN, and (d) NNA models. True classes (*Y*-axis) represent the already trained (labeled) values introduced to the models and predicted classes (*X*-axis) are the calculated results by the model. The discrimination accuracy is 100% for all three models.

they quickly reached saturation and returned to their initial background values in 10 min. The NH_2-functionalized UiO-66-X sensor demonstrated higher responses (more than two times) than the N_3- and Cl-functionalized sensors. The Cl-functionalized sensor had slightly more responses than the N_3-functionalized one. All three sensors showed the highest response to water, methanol, and ethanol, while lower responses were found to toluene and *n*-hexane.

Adsorption Measurements under Low Concentrations (10−100 ppm). The second measurement was taken at six low concentrations (10, 15, 25, 50, 75, and 100 ppm) to examine the lowest sensing limit of the functional UiO-66-X SURMOF sensor films. The gas injection time was again chosen to be 10 min for adsorption, but the Ar rinsing time was increased to 20 min for desorption to test the sensor response time. Figure S4 illustrates the QCM responses of three functional UiO-66-X (X = NH_2, X = Cl, and X = N_3) against *p*-xylene (Figure S4a−c), water (Figure S4d−f), toluene (Figure S4g−I), ethanol (Figure S4i−k), 2-propanol (Figure S4l−n), *n*-hexane (Figure S4o−r), cyclohexane (Figure S4v−z) at low concentrations between 10 and 100 ppm.

The sensitivities of each UiO-66-X sensor can be defined as the slopes of the plots with QCM frequency changes versus concentration for each sensor response, as shown in Table S1. Each sensor had a different slope for different gas molecules as the SURMOF material was loaded with different concentrations and functional groups.

The sensitivities of the UiO-66-NH_2 sensor for 2-propanol, cyclohexane, ethanol, *n*-hexane, methanol, toluene, water, and *p*-xylene were 0.0028, 0.0024, 0.0055, 0.0007, 0.0025, 0.0036, 0.0169, and 0.0108 Hz/ppm, respectively. The highest sensitivity of 0.0169 Hz/ppm was observed to water among all functional UiO-66-X sensors, as given in Table S1b. UiO-66-NH_2 was more sensitive than other functionalized sensors. *p*-Xylene exhibited the second highest sensitivity (0.0108 Hz/ppm). The sensitivity was in the range of 0.0004−0.0067 Hz/ppm for UiO-66-Cl sensors and 0.0006−0.0090 Hz/ppm for UiO-66-N_3 sensors. The lowest sensitivity was observed for *n*-hexane (0.0004 Hz/ppm), followed by cyclohexane (0.0011 Hz/ppm) for the UiO-66-Cl sensors. The same UiO-66-X sensor showed different sensitivities depending on the analytes due to the different affinities derived from various functional groups. This feature is important for distinguishing the analytes via ML methods such as LDA, *k*-NN, and NNA.

The limits of detection (LOD) of individual sensors (Table S1) were calculated by three times the standard deviation divided by sensitivity. For standard deviations of the signals, we used the average value of the standard deviation of each individual sensor, determined from the baselines before the analyte exposure began. The average values of the standard deviations were 0.23 Hz for the UiO-66-NH_2 sensor, 0.10 for the UiO-66-Cl sensor, and 0.28 for the UiO-66-N_3 sensor. The UiO-66-Cl sensor exhibited the lowest LOD due to the lowest standard deviation. The lowest detection limits depended on the type of analytes and were around 50 ppm for most VOCs. The obtained LOD values of the present sensor are similar compared to some published sensors for alcohol vapors, as shown in Table S2. As previously mentioned, the mass sensitivity constant C depends solely on the fundamental resonance frequency f_0 and the material properties of the quartz crystal. Accordingly, LOD depends not only on the affinity of the functional groups of UiO-66-X films but also on the driving resonance frequency of underlying QCM oscillator sensors.[34,35] Consequently, using thinner QCM oscillator

sensors with higher resonance frequencies, the LOD can decrease under the ppm level for lower concentrations.

E-Nose Discrimination Analysis. The response of functionalized UiO-66-X sensors differs for each VOC, thus acting as a fingerprint for each gas type for use in e-nose applications. The discrimination analysis used three models: LDA,[16,22] in which the ratio of variances between classes and inside the classes is maximized; *k*-NN,[23] using a $k = 10$ nearest neighbor model where an unknown data point is classified according to the nearest distance of its 10 nearest neighbors; and NNA,[38−40] using a single hidden layer with 25 sizes and lambda zero, rectified linear unit (ReLU) activation function, and standardized data. E-nose discrimination analysis was applied to both adsorption data under the saturated vapor pressure of VOCs and at six low concentrations between 10 and 100 ppm.

The data taken from a saturated region of the adsorption/desorption curves given in Figure 5 were used for the discrimination analysis of the VOC data. A 10-fold cross-validation threshold was employed for classification using 4638 individual observations. Typically, 10% of the data was set aside for testing. Consequently, 4175 observations were used for the training set, and 463 were utilized for comparing the discrimination accuracies obtained with LDA, *k*-NN, and NNA models separately.

Figure 5a illustrates a two-dimensional visual discrimination plot of LDA analysis with a 95% confidence ellipse of eight VOCs, including water, at their saturated vapor pressure concentrations. Typically, 96.3% discrimination was obtained in the first LDA component, and 3.1% discrimination was obtained in the second LDA component. The confusion matrix results of the LDA model with 100% test discrimination accuracy are given in Figure 5b. With the *k*-NN model, 100% discrimination accuracy was calculated, as displayed in Figure 5c. In addition, 100% discrimination accuracy was obtained with the NNA model, with the confusion matrix presented in Figure 5d.

The functional UiO-66-X (X = NH_2, Cl, and N_3) sensors were also tested under six low concentrations (10, 15, 25, 50, 75, and 100 ppm). During e-nose analysis with all three models (LDA, *k*-NN, and NNA), 10-fold calculations were conducted for all low concentrations between 10 and 100 ppm. For example, 10 test sets were used with 1780 observations (1602 training size and 178 test size). Here, only the analysis results of 25 and 100 ppm e-nose measurements are presented for comparison.

Figure S5 displays the e-nose analysis of the functional UiO-66-X sensor array at 25 ppm using three models: LDA, *k*-NN ($k = 10$), and NNA (with 25 single hidden layer size and ReLU activation). Figure S5a illustrates two-dimensional plots of LDA with a 95% confidence ellipse of frequency changes of three functional UiO-66-X sensors against all eight VOC analytes, including water vapor, at 25 ppm. Typically, 88.7% discrimination accuracy was obtained with LDA, with the confusion matrix given in Figure S5b. The discrimination with 96.1% accuracy was obtained from the *k*-NN model, and the confusion matrix is given in Figure S5c. With the NNA model, 96.2% discrimination accuracy was obtained and the confusion matrix is given in Figure S5d. The highest discrimination accuracy was obtained using the NNA model.

Figure S6 displays the e-nose analysis of the functional UiO-66-X sensor array at 100 ppm by using three models: LDA, *k*-NN ($k = 10$), and NNA (with 100 single hidden layer size and RELU activation). Figure S6a illustrates two-dimensional plots of LDA with a 95% confidence ellipse of frequency changes of three functional UiO-66-X sensors against all eight VOC analytes, including water vapor, at 100 ppm. Typically, 90.0% discrimination accuracy was obtained with LDA with the confusion matrix given in Figure S6b. Discrimination with 99.9% accuracy was obtained from the *k*-NN model, and the confusion matrix is given in Figure S6c. With the NNA model, 99.6% discrimination accuracy was obtained, and the confusion matrix is given in Figure S6d. The highest discrimination accuracy was obtained using the *k*-NN model at 100 ppm.

Figure 6 displays the change in discrimination accuracy of the three models with increasing concentrations from 10 to 100 ppm. The LDA discrimination accuracy increased from 74.8 to 98.4%, while the *k*-NN discrimination accuracy increased from 89.9 to 100%. An increase was observed in concentrations up to 100 ppm for all three models. However, *k*-NN and NNA revealed higher discrimination accuracies compared to LDA.

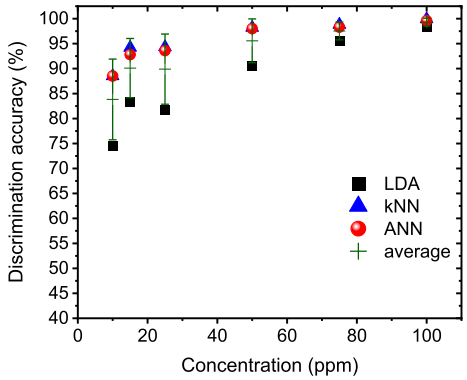

Figure 6. Change in the discrimination accuracy of LDA, *k*-NN, and NNA models with increasing concentration from 10 to 100 ppm.

Classification models such as LDA, *k*NN, and ANN help to discriminate the responses of a sensor array to different VOC vapors or even different low concentrations, up to 10 ppm in this work. UIO-66-X is one of the most stable MOF structures, with a very prominent zirconia cluster in the center with one large pore and 8 small pores allowing selectivity for the VOC molecules according to their size and affinity. Here, we see that those classification models can be used for QCM-type e-nose applications with only three different functional groups from the same highly stable UIO-66 SURMOF sensor array. The greater the difference in the type of sensing response to the same VOC odor, the greater the selectivity. Therefore, the selectivity of the SURMOF sensor array used for e-nose applications can be easily increased by adding another functional group to the sensor array with the PMS techniques proposed in this work.

Sensor selectivity and discrimination accuracy of the e-nose can be improved further by utilizing other types of functional groups.

Highly stable UiO-66-X SURMOFs can be easily post-modified for this purpose. Figure 7 and Table S2 show a possible postmodification of UiO-66-NH_2 to add several different functional groups according to needs of industrial applications.

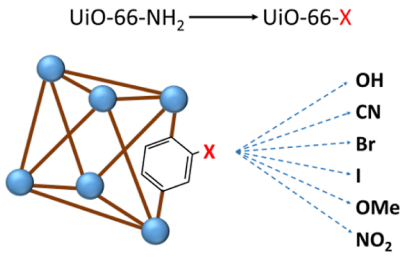

Figure 7. Possible postmodification of UiO-66-NH_2 to add different functional groups.

CONCLUSIONS

We introduced a novel gravimetric, MOF-based sensor platform based on UiO-66-X. Different variants of the UiO-66-family of MOF thin films, or SURMOFs, were obtained by PSM of a parent UiO-66-NH_2 SURMOF. As a proof of principle, three different sensors with X = NH_2, Cl, and N_3 were coupled to an array to detect and differentiate eight different VOCs. The UiO-66-based sensors showed high stability and survived harsh conditions, e.g., operation at 100% RH and 90 °C and even inside water at pH values from 1 to 7 and 20 °C.

The analysis of the sensor array was carried out using three different ML methods: LDA, *k*-NN, and NNA. Close to 100% discrimination accuracy was obtained at saturated vapor pressure. At low concentrations between 10 and 100 ppm, the obtained discrimination accuracies were between 74.8 and 99.9%. The lowest detection limits depended on the type of analyte and were between 19 and 440 ppm for most VOCs. However, using QCM oscillator sensors with higher resonance frequencies, LOD can be decreased under the ppm level of the concentrations since the mass sensitivity of QCM sensors depends on the square of the driving fundamental resonance frequency of the QCM resonator circuit.

Our results demonstrate that QCM-based sensors employing UiO-66-NH_2 SURMOFs represent a very versatile, robust, and sensitive platform for VOC detection. High sensitivity for target VOC can be obtained by suitable functionalization of the NH_2 side groups in UiO-66-NH_2. In the present case, with only three different side groups, a total of eight different VOCs could be reliably detected and differentiated. For further VOCs, other side groups can be employed, such as Br, I, OH, CN, OMe, and NO_2. With regard to applications of chiral VOCs (e.g., biomolecules), we also foresee the use of click-chemistry[41−43] to couple short peptides to the UiO-66-N_3 parent MOF, thus rendering the possibility of differentiating between different enantiomers[16,44] using our e-nose.

AUTHOR INFORMATION

Corresponding Author

Christof Wöll − *Karlsruhe Institute of Technology (KIT), Institute of Functional Interfaces, 76344 Eggenstein-Leopoldshafen, Germany;* orcid.org/0000-0003-1078-3304; Email: christof.woell@kit.edu

Authors

Salih Okur − *Karlsruhe Institute of Technology (KIT), Institute of Functional Interfaces, 76344 Eggenstein-Leopoldshafen, Germany*

Tawheed Hashem − *Karlsruhe Institute of Technology (KIT), Institute of Functional Interfaces, 76344 Eggenstein-Leopoldshafen, Germany*

Evgenia Bogdanova − *Karlsruhe Institute of Technology (KIT), Institute of Functional Interfaces, 76344 Eggenstein-Leopoldshafen, Germany*

Patrick Hodapp − *Karlsruhe Institute of Technology (KIT), Institute for Biological Interfaces 3−Soft Matter Synthesis Laboratory (IBG3−SML), 76131 Karlsruhe, Germany*

Lars Heinke − *Karlsruhe Institute of Technology (KIT), Institute of Functional Interfaces, 76344 Eggenstein-Leopoldshafen, Germany;* orcid.org/0000-0002-1439-9695

Stefan Bräse − *Karlsruhe Institute of Technology (KIT), Institute of Organic Chemistry (IOC), 76131 Karlsruhe, Germany; Karlsruhe Institute of Technology (KIT), Institute of Biological and Chemical Systems−Functional Molecular Systems (IBCS−FMS), 76131 Karlsruhe, Germany;* orcid.org/0000-0003-4845-3191

Author Contributions

‖ S.O. and T.H. equal contribution.

Notes

The authors declare no competing financial interest.

ACKNOWLEDGMENTS

S.O., T.H., S.B., and C.W. acknowledge support through the Deutsche Forschungsgemeinschaft (DFG) within the Cluster "3DMM2O" funded by Germany's Excellence Strategy −2082/1−390761711.

REFERENCES

(1) Bon, V.; Brunner, E.; Pöppl, A.; Kaskel, S. Unraveling structure and dynamics in porous frameworks via advanced in situ characterization techniques. *Adv. Funct. Mater.* **2020**, *30* (41), 1907847.

(2) Gandara-Loe, J.; Pastor-Perez, L.; Bobadilla, L.; Odriozola, J.; Reina, T. Understanding the opportunities of metal-organic frameworks (MOFs) for CO 2 capture and gas-phase CO 2 conversion processes: a comprehensive overview. *React. Chem. Eng.* **2021**, *6* (5), 787−814.

(3) von Helden, G.; van Heijnsbergen, D.; Meijer, G. Resonant ionization using IR light: A new tool to study the spectroscopy and dynamics of gas-phase molecules and clusters. *J. Phys. Chem. A* **2003**, *107* (11), 1671−1688.

(4) Silva, P.; Vilela, S. M.; Tome, J. P.; Almeida Paz, F. A. Multifunctional metal-organic frameworks: from academia to industrial applications. *Chem. Soc. Rev.* **2015**, *44* (19), 6774−6803.

(5) Liu, J.; Wöll, C. Surface-supported metal-organic framework thin films: fabrication methods, applications, and challenges. *Chem. Soc. Rev.* **2017**, *46* (19), 5730−5770.

(6) Wang, C.; Liu, D.; Lin, W. Metal-organic frameworks as a tunable platform for designing functional molecular materials. *J. Am. Chem. Soc.* **2013**, *135* (36), 13222−13234.

(7) Eddaoudi, M.; Moler, D. B.; Li, H.; Chen, B.; Reineke, T. M.; O'keeffe, M.; Yaghi, O. M. Modular chemistry: secondary building units as a basis for the design of highly porous and robust metal-organic carboxylate frameworks. *Acc. Chem. Res.* **2001**, *34* (4), 319−330.

(8) Li, Y.; Wen, G.; Li, J.; Li, Q.; Zhang, H.; Tao, B.; Zhang, J. Synthesis and shaping of metal-organic frameworks: a review. *Chem. Commun.* **2022**, *58* (82), 11488−11506.
(9) Ahmadi, M.; Ebrahimnia, M.; Shahbazi, M.-A.; Keçili, R.; Ghorbani-Bidkorbeh, F. Microporous metal-organic frameworks: Synthesis and applications. *J. Ind. Eng. Chem.* **2022**, *115*, 1−11.
(10) Altaf, A.; Hassan, S.; Pejcic, B.; Baig, N.; Hussain, Z.; Sohail, M. Recent progress in the design, synthesis and applications of chiral metal-organic frameworks. *Front. Chem.* **2022**, *10*, 1014248.
(11) Chen, D.-H.; Gliemann, H.; Wöll, C. Layer-by-layer assembly of metal-organic framework thin films: Fabrication and advanced applications. *Chem. Phys. Rev.* **2023**, *4* (1), 011305.
(12) Lee, T.; Liu, Z. X.; Lee, H. L. A Biomimetic Nose by Microcrystals and Oriented Films of Luminescent Porous Metal-Organic Frameworks. *Cryst. Growth Des.* **2011**, *11* (9), 4146−4154.
(13) Qin, L.; Wang, X.; Liu, Y.; Wei, H. 2D-Metal-Organic-Framework-Nanozyme Sensor Arrays for Probing Phosphates and Their Enzymatic Hydrolysis. *Anal. Chem.* **2018**, *90* (16), 9983−9989.
(14) Campbell, M. G.; Liu, S. F.; Swager, T. M.; Dincă, M. Chemiresistive Sensor Arrays from Conductive 2D Metal-Organic Frameworks. *J. Am. Chem. Soc.* **2015**, *137* (43), 13780−13783.
(15) Hu, W.; Wan, L.; Jian, Y.; Ren, C.; Jin, K.; Su, X.; Bai, X.; Haick, H.; Yao, M.; Wu, W. Electronic Noses: From Advanced Materials to Sensors Aided with Data Processing. *Adv. Mater. Technol.* **2019**, *4* (2), 1800488.
(16) Okur, S.; Qin, P.; Chandresh, A.; Li, C.; Zhang, Z.; Lemmer, U.; Heinke, L. An enantioselective e-nose: an array of nanoporous homochiral MOF films for stereospecific sensing of chiral odors. *Angew. Chem., Int. Ed.* **2021**, *60* (7), 3566−3571.
(17) Li, H.; Wang, L.; Yan, S.; Chen, J.; Zhang, M.; Zhao, R.; Niu, X.; Wang, K. Fusiform-like metal-organic framework for enantioselective discrimination of tryptophan enantiomers. *Electrochim. Acta* **2022**, *419*, 140409.
(18) Satska, Y. A.; Mikhalyova, E. A.; Chernenko, Z. V.; Kolotilov, S. V.; Zeller, M.; Komarov, I. V.; Tymtsunik, A. V.; Tolmachev, A.; Gavrilenko, K. S.; Addison, A. W. Sorption discrimination between secondary alcohol enantiomers by chiral alkyl-dicarboxylate MOFs. *RSC Adv.* **2016**, *6* (96), 93707−93714.
(19) Hashem, T.; Valadez Sánchez, E. P.; Weidler, P. G.; Gliemann, H.; Alkordi, M. H.; Wöll, C. Liquid-Phase Quasi-Epitaxial Growth of Highly Stable, Monolithic UiO-66-NH_2 MOF thin Films on Solid Substrates. *ChemistryOpen* **2020**, *9* (5), 524−527.
(20) Yang, X.-L.; Zang, R.-B.; Shao, R.; Guan, R.-F.; Xie, M.-H. Chiral UiO-MOFs based QCM sensors for enantioselective discrimination of hazardous biomolecule. *J. Hazard. Mater.* **2021**, *413*, 125467.
(21) Wang, L. Metal-organic frameworks for QCM-based gas sensors: A review. *Sens. Actuators, A* **2020**, *307*, 111984.
(22) Okur, S.; Zhang, Z.; Sarheed, M.; Nick, P.; Lemmer, U.; Heinke, L. Towards a MOF e-Nose: A SURMOF sensor array for detection and discrimination of plant oil scents and their mixtures. *Sens. Actuators, B* **2020**, *306*, 127502.
(23) Qin, P.; Okur, S.; Li, C.; Chandresh, A.; Mutruc, D.; Hecht, S.; Heinke, L. A photoprogrammable electronic nose with switchable selectivity for VOCs using MOF films. *Chem. Sci.* **2021**, *12* (47), 15700−15709.
(24) Zhang, L. T.; Zhou, Y.; Han, S. T. The role of metal-organic frameworks in electronic sensors. *Angew. Chem.* **2021**, *133* (28), 15320−15340.
(25) Feng, L.; Wang, K.-Y.; Day, G. S.; Ryder, M. R.; Zhou, H.-C. Destruction of metal-organic frameworks: positive and negative aspects of stability and lability. *Chem. Rev.* **2020**, *120* (23), 13087−13133.
(26) Binaeian, E.; El-Sayed, E.-S. M.; Khanpour Matikolaei, M.; Yuan, D. Experimental strategies on enhancing toxic gases uptake of metal-organic frameworks. *Coord. Chem. Rev.* **2021**, *430*, 213738.
(27) Younas, M.; Rezakazemi, M.; Daud, M.; Wazir, M. B.; Ahmad, S.; Ullah, N.; Ramakrishna, S. Recent progress and remaining challenges in post-combustion CO2 capture using metal-organic frameworks (MOFs). *Prog. Energy Combust. Sci.* **2020**, *80*, 100849.
(28) Tzoulaki, D.; Heinke, L.; Lim, H.; Li, J.; Olson, D.; Caro, J.; Krishna, R.; Chmelik, C.; Kärger, J. Assessing surface permeabilities from transient guest profiles in nanoporous host materials. *Angew. Chem., Int. Ed.* **2009**, *48* (19), 3525−3528.
(29) Nijem, N.; Fürsich, K.; Kelly, S. T.; Swain, C.; Leone, S. R.; Gilles, M. K. HKUST-1 Thin Film Layer-by-Layer Liquid Phase Epitaxial Growth: Film Properties and Stability Dependence on Layer Number. *Cryst. Growth Des.* **2015**, *15* (6), 2948−2957.
(30) Hashem, T.; Sanchez, E. P. V.; Bogdanova, E.; Ugodchikova, A.; Mohamed, A.; Schwotzer, M.; Alkordi, M. H.; Wöll, C. Stability of Monolithic MOF Thin Films in Acidic and Alkaline Aqueous Media. *Membranes* **2021**, *11* (3), 207.
(31) Micero, A.; Hashem, T.; Gliemann, H.; Léon, A. Hydrogen Separation Performance of UiO-66-NH_2 Membranes Grown via Liquid-Phase Epitaxy Layer-by-Layer Deposition and One-Pot Synthesis. *Membranes* **2021**, *11* (10), 735.
(32) Shultz, A. M.; Sarjeant, A. A.; Farha, O. K.; Hupp, J. T.; Nguyen, S. T. Post-synthesis modification of a metal-organic framework to form metallosalen-containing MOF materials. *J. Am. Chem. Soc.* **2011**, *133* (34), 13252−13255.
(33) Thomson, G. W. The Antoine Equation for Vapor-pressure Data. *Chem. Rev.* **1946**, *38* (1), 1−39.
(34) Sauerbrey, G. Z. Use a quartz vibration form weigh thin films on a microbalance. *Z. Phys.* **1959**, *155*, 206−210.
(35) Reviakine, I.; Johannsmann, D.; Richter, R. P. Hearing What You Cannot See and Visualizing What You Hear: Interpreting Quartz Crystal Microbalance Data from Solvated Interfaces. *Anal. Chem.* **2011**, *83* (23), 8838−8848.
(36) Okur, S.; Sarheed, M.; Huber, R.; Zhang, Z.; Heinke, L.; Kanbar, A.; Wöll, C.; Nick, P.; Lemmer, U. Identification of mint scents using a QCM based e-nose. *Chemosensors* **2021**, *9* (2), 31.
(37) Hashem, T.; Ibrahim, A. H.; Wöll, C.; Alkordi, M. H. Grafting Zirconium-Based Metal-Organic Framework UiO-66-NH_2 Nanoparticles on Cellulose Fibers for the Removal of Cr(VI) Ions and Methyl Orange from Water. *ACS Appl. Nano Mater.* **2019**, *2* (9), 5804−5808.
(38) Yu, H.; Wang, J.; Yao, C.; Zhang, H.; Yu, Y. Quality grade identification of green tea using E-nose by CA and ANN. *LWT−Food Sci. Technol.* **2008**, *41* (7), 1268−1273.
(39) Wilson, A. D.; Baietto, M. Applications and Advances in Electronic-Nose Technologies. *Sensors* **2009**, *9* (7), 5099−5148.
(40) Saraoğlu, H. M.; Edin, B. E-Nose system for anesthetic dose level detection using artificial neural network. *J. Med. Syst.* **2007**, *31* (6), 475−482.
(41) Devaraj, N. K.; Finn, M. *Introduction: Click Chemistry*; ACS Publications, 2021; Vol. *121*, pp 6697−6698.
(42) Kumar, G. S.; Lin, Q. Light-triggered click chemistry. *Chem. Rev.* **2021**, *121* (12), 6991−7031.
(43) Moharramnejad, M.; Ehsani, A.; Shahi, M.; Gharanli, S.; Saremi, H.; Malekshah, R. E.; Basmenj, Z. S.; Salmani, S.; Mohammadi, M. MOF as nanoscale drug delivery devices: Synthesis and recent progress in biomedical applications. *J. Drug Delivery Sci. Technol.* **2023**, *81*, 104285.
(44) Qin, P.; Day, B. A.; Okur, S.; Li, C.; Chandresh, A.; Wilmer, C. E.; Heinke, L. VOC mixture sensing with a MOF film sensor array: Detection and discrimination of Xylene Isomers and their Ternary Blends. *ACS Sens.* **2022**, *7* (6), 1666−1675.